



HAL
open science

A New Cyclo-Synchrotron Model for Lunar-Based Observations of Earth's Radiation Belts

Gwendoline Marc, Angélica Sicard, Quentin Nénon, Renaud Belmont

► **To cite this version:**

Gwendoline Marc, Angélica Sicard, Quentin Nénon, Renaud Belmont. A New Cyclo-Synchrotron Model for Lunar-Based Observations of Earth's Radiation Belts. *Journal of Geophysical Research Space Physics*, 2024, 129 (10), pp.e2024JA032563. 10.1029/2024ja032563 . hal-04733024

HAL Id: hal-04733024

<https://hal.science/hal-04733024v1>

Submitted on 11 Oct 2024

HAL is a multi-disciplinary open access archive for the deposit and dissemination of scientific research documents, whether they are published or not. The documents may come from teaching and research institutions in France or abroad, or from public or private research centers.

L'archive ouverte pluridisciplinaire **HAL**, est destinée au dépôt et à la diffusion de documents scientifiques de niveau recherche, publiés ou non, émanant des établissements d'enseignement et de recherche français ou étrangers, des laboratoires publics ou privés.



Distributed under a Creative Commons Attribution 4.0 International License

JGR Space Physics

RESEARCH ARTICLE

10.1029/2024JA032563

Key Points:

- A new model of the radio signal emitted by the terrestrial radiation belts and seen by a lunar observer is developed
- The model relies on the full cyclo-synchrotron formalism to extend previous work to electron energies lower than 1 MeV

Correspondence to:

G. Marc,
gwendoline.marc@onera.fr



Citation:

Marc, G., Sicard, A., Nénon, Q., & Belmont, R. (2024). A new cyclo-synchrotron model for lunar-based observations of Earth's radiation belts. *Journal of Geophysical Research: Space Physics*, 129, e2024JA032563. <https://doi.org/10.1029/2024JA032563>

Received 19 FEB 2024

Accepted 11 SEP 2024

A New Cyclo-Synchrotron Model for Lunar-Based Observations of Earth's Radiation Belts

G. Marc¹ , A. Sicard¹, Q. Nénon² , and R. Belmont³

¹DPHY, ONERA, Université de Toulouse, Toulouse, France, ²Institut de Recherche en Astrophysique et Planétologie, CNRS-UPS-CNES, Toulouse, France, ³CEA Saclay, IRFU/DAP, Gif-sur-Yvette, France

Abstract The energetic electrons trapped in the terrestrial radiation belts spontaneously emit radiation due to magnetic deflection. The observation of this radiation can offer insights into the space and energy distribution of the electrons, as well as their temporal variability. Given the energy range of the electrons in the Earth's radiation belts (0.1 keV to 10 MeV), the emission corresponds to cyclo-synchrotron radiation, an intermediate radiation regime between the low-energy cyclotron radiation and the extremely relativistic synchrotron emission. Terrestrial cyclo-synchrotron radiation cannot be observed from Earth as it is emitted at frequencies below the ionospheric cutoff frequency ($f < 10$ MHz). However, a lunar near-side observation could provide real time measurements of the dynamics of the Earth radiation belts. In this study, we present the development of a full cyclo-synchrotron model for the electron radiation belt emissions, building upon a preliminary synchrotron model. While previous simulations focused on >1 MeV electrons, our new model is able to simulate the radiation of >100 keV electrons which have much larger fluxes than MeV electrons. This new model accurately simulates the cyclo-synchrotron radiation emitted by Earth's radiation belts as observed from the lunar surface, which would help the design of lunar-based radio interferometers and would offer a new perspective on radiation belts research and monitoring.

1. Introduction

The Earth's radiation belts pose a significant threat to space operations, even during relatively calm periods. Their dynamics are characterized by high-energy particle flux that can vary by several orders of magnitude within a few hours. Satellites traveling through these regions are prone to both short-term disruptions and long-term degradation. Currently, most satellites orbit within these radiation belts, putting them at the forefront during geomagnetic storms. Damage to onboard electronics is a common issue for Earth-orbiting satellites, and the occurrence of these anomalies is directly related to the increased proton and electron fluxes during magnetic storms (Horne et al., 2013). Consequently, observing and monitoring energetic particles across the radiation belts is crucial. However, the existing approach relies exclusively on onboard particle detectors, resulting in limited spatial coverage and an incomplete insight of the belts' temporal fluctuations.

Relativistic electrons trapped in radiation belts experience deflection due to the planet's magnetic field and subsequently emit synchrotron radiation. To date, only the radiation belts of Jupiter have been confirmed to exhibit this phenomenon in the solar system (Carr et al., 1983; de Pater, 1981; Grießmeier et al., 2011; Girard et al., 2016 and references therein). These observations have significantly contributed to our comprehension of the dynamics of energetic electrons close to Jupiter (Nénon et al., 2017; Santos-Costa et al., 2008; Sicard et al., 2004).

However, terrestrial radiation is expected to be emitted at frequencies between 0.01 and 10 MHz (Hegedus et al., 2020) and cannot be observed by ground-based instruments due to the ionospheric cut-off limitations at $f < 10$ MHz (de Pater & Kurth, 2007). Previously, Hegedus et al. (2020) carried out a preliminary study proposing a solution to this problem: setting up a radio interferometer on the lunar near side surface. The use of such an instrument to generate 2D maps of the electron emissions holds the promise of revealing the spatial and energy distribution of Earth's radiation belt electrons, ultimately providing global coverage of the radiation belts. In their work, Hegedus et al. (2020) presented the results of simulations of the synchrotron radiation emitted by electrons with a kinetic energy greater than 1 MeV, therefore considering only relativistic electrons.

While MeV to GeV electrons trapped in the Jovian radiation belts can be considered fully relativistic, this characterization does not apply to electrons in Earth's radiation belts, which typically have energies between 10 keV and 1 MeV. The synchrotron formalism is suited for the Jovian context but may not be directly applicable

©2024. The Author(s).

This is an open access article under the terms of the [Creative Commons Attribution License](https://creativecommons.org/licenses/by/4.0/), which permits use, distribution and reproduction in any medium, provided the original work is properly cited.

to Earth's radiation belts (Rybicki & Lightman, 1979). Instead, the cyclo-synchrotron formalism, which describes emissions from electrons at lower energy levels, is a more appropriate approach for Earth's radiation belts. The new cyclo-synchrotron model presented in this paper enables us to consider both non-relativistic and relativistic electrons and provide a more accurate insight of emission intensity as observed from the Moon. While several codes have been developed across different domains for simulating cyclo-synchrotron (gyro-synchrotron) emissions (Kuznetsov & Fleishman, 2021), we chose to adapt an existing, validated synchrotron code specifically for studying the Earth's radiation belts. This approach offered a solid foundation, enabling a more efficient development process.

This paper is structured as follows: Section 2 introduces the synchrotron and cyclo-synchrotron equations. In Section 3, the equations used to calculate the power emitted by a population of radiation belt electrons as perceived from the lunar surface are presented. Section 4 discusses the results and conducts a comparative analysis between synchrotron and cyclo-synchrotron models. Finally, we conclude by outlining directions for future research work.

2. Theory: Synchrotron and Cyclo-Synchrotron Radiation of an Accelerated Electron

2.1. Emission From Charged Particles

Maxwell's laws show that a charged particle that undergoes acceleration spontaneously emits photons. The power emitted by such a particle at low velocity ($v \ll c$) exhibits a distinctive two-lobe distribution pattern represented in Figure 1 for $\beta = \frac{v}{c} = 0.2$. In a non-relativistic case, the emission is known as 'cyclotron radiation'.

When a particle is relativistic ($v \sim c$), the Lorentz transform of the cyclotron radiation from the particle rest frame to the observer reference frame shows that the emission is seen by the observer as strongly beamed along the direction of particle motion, as presented in Figure 1 for $\beta = 0.99$. The main emission power is concentrated within an angle of order $2/\gamma$ where γ is the particle Lorentz factor defined as $\gamma = \frac{1}{\sqrt{1-\beta^2}}$. As the electrons spiral around magnetic field lines, a distant observer can perceive the emission only when the beam is aligned at $\pm 1/\gamma$ with the observer's line of sight.

The angular distributions presented in Figure 1 is calculated with the following equation:

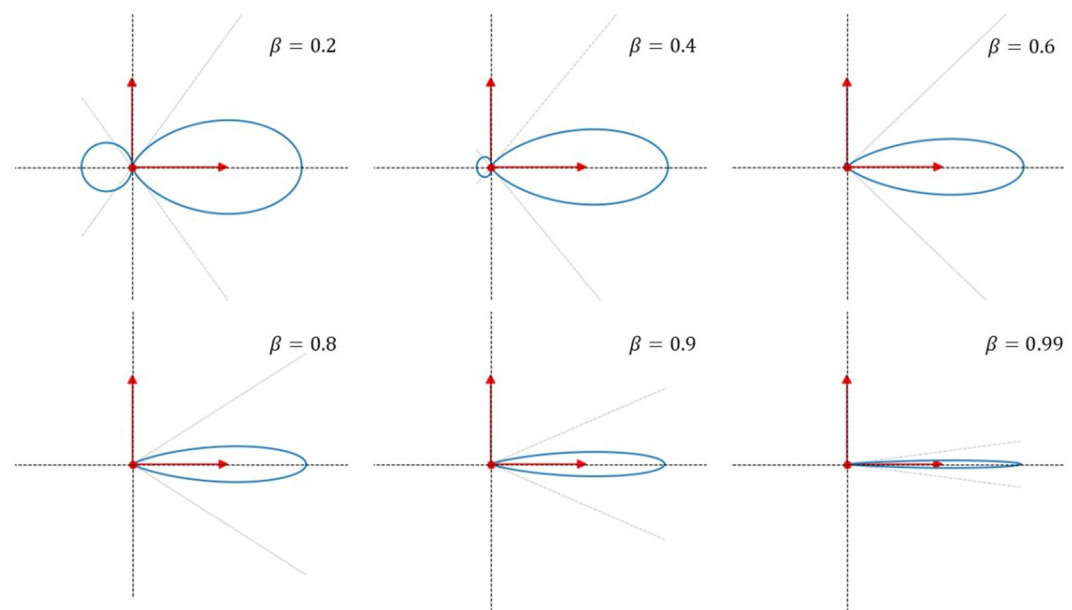


Figure 1. Emission diagram for particles with a velocity between $\beta = 0.2$ (non-relativistic) and $\beta = 0.99$ (ultra-relativistic).

$$\frac{dP}{d\Omega} \frac{4\pi c}{e^2 \beta^2} = \frac{\gamma^2 (1 - \beta \cos(\theta))^2 - \sin(\theta)^2}{\gamma^2 (1 - \beta) \cos(\theta)^5} \quad (1)$$

Where $\vec{\beta} = \frac{\vec{v}}{c}$, $\dot{\vec{\beta}} = \frac{d\vec{\beta}}{dt}$, \vec{n} the direction of observation and P the emitted power.

The angular distribution of the radiation has a significant impact on the observed frequency spectrum.

For an electron with mass m_0 and charge e embedded in a magnetic field of intensity B the observed spectrum consists of multiple harmonic lines with the fundamental frequency f_B as:

$$f_B = \frac{f_L}{\gamma}, \quad f_L = \frac{eB}{2\pi m_0} \text{ [Hz]} \quad (2)$$

With f_L the cyclotron frequency.

When $\beta \sim 0$, $\gamma \sim 1$, the spectrum is reduced to a single delta function at $f_B \sim f_L$. As β increases, higher harmonics of the fundamental frequency f_B contribute to the observed signal (see Section 2.3). When $\beta \sim 1$, the spectrum is composed of successive delta functions close in frequency, approximating a continuous spectrum.

2.2. The Synchrotron Approximation

The frequency spectrum of the power received by an observer, noted Pf , and emitted by an ultra-relativistic electron spiraling in a magnetic field B is a frequency continuum given by (Rybicki & Lightman, 1979; Schwinger, 1949):

$$Pf = \frac{\sqrt{3}e^3}{4\pi m_0 c} B \sin(\alpha) F(X) \text{ [W.Hz}^{-1}] \quad (3)$$

Where

$$X = \frac{f}{f_c}, \quad f_c = \frac{3eB}{4\pi m_0} \gamma^2 \sin(\alpha) \quad (4)$$

And

$$F(X) = X \int_X^\infty K_{5/3}(\xi) d\xi \quad (5)$$

With $K_{5/3}(\xi)$ the modified Bessel function of order 5/3 and α the electron pitch angle corresponding to the angle between the velocity vector and the magnetic field line. In Formula 3, α is also the observer angle (noted θ hereafter, it is the angle between the observer line of sight and the magnetic field vector) because the observer can only observe electrons with $\alpha = \theta$ in the ultrarelativistic regime. However, while the synchrotron approximation is valid for ultra-relativistic electrons, the modeling of lower energy electrons trapped in the radiation belts require the computation of the full cyclo-synchrotron radiation (e.g., Marcowith & Malzac, 2003).

2.3. Cyclo-Synchrotron Radiation

The power emitted by a single electron with a pitch angle α and for an observer angle θ , the angle between the observer direction and the magnetic field, is given by the Schott formula (e.g., Marcowith & Malzac, 2003; Schott, 1912; Schwinger, 1949; Wolfe and Melia, 2006):

$$\frac{\partial^2 P}{\partial \Omega \partial f} = \frac{P_0}{f_L} \frac{9}{8\pi} \frac{\sin(\alpha)^2}{\gamma} \sum_{n=1}^{\infty} \frac{1}{n} \left[\left(\frac{\cos(\theta) - \beta \cos(\alpha)}{1 - \beta \cos(\theta) \cos(\alpha)} \right)^2 \left(\frac{n J_n(x)}{x} \right)^2 + J_n'(x)^2 \right] \delta(y) \text{ [W.Hz}^{-1}.str^{-1}] \quad (6)$$

P_0 corresponds to the total power emitted by an accelerating charged particle. It is calculated using the Larmor formula: $P_0 = \frac{2}{3} \frac{e^4 B^2 \beta^2 \gamma^2}{4\pi\epsilon_0 m_0^2 c^3}$ (SI units).

For a given harmonic n , emission occurs exclusively at the resonance frequency f_{res} as:

$$y = \frac{f_{res}}{f_L} - \frac{n}{(1 - \cos \theta \cos \alpha)\gamma} = 0 \quad (7)$$

Hence

$$f_{res} = \frac{nf_L}{\gamma(1 - \cos \theta \cos \alpha)} = \frac{nf_B}{(1 - \cos \theta \cos \alpha)} [Hz] \quad (8)$$

In Equation 5, x is given by:

$$x = \frac{f_{res}}{f_L} \gamma \beta_{\perp} \sin \theta \quad (9)$$

The Schott formula is valid for all electron kinetic energies. In particular, the cyclotron and synchrotron approximations can be retrieved from the cyclo-synchrotron formalism. The nature of this emission is discrete, which represents a real numerical challenge. For each observation frequency of interest, we sum emissions from all harmonic frequencies in an interval $\left[\frac{f_{obs}}{f_L} - \Delta f; \frac{f_{obs}}{f_L} + \Delta f\right]$ with $\Delta f = \epsilon \frac{f_{obs}}{f_L}$. For our calculation, we follow the method of Marcowith and Malzac (2003) and set $\epsilon = 0.05$, which enables us to broaden the delta functions sufficiently to achieve accurate results without compromising the harmonic structure. Equation 6 can be normalized by f_L/P_0 and becomes:

$$\frac{\partial^2(P/P_0)}{\partial\Omega\partial(f/f_L)} = \frac{9}{8\pi} \frac{\sin(\alpha)^2}{\gamma\Delta f} \sum_{n=n_1}^{n_2} \frac{1}{n} \left[\left(\frac{\cos(\theta) - \beta \cos(\alpha)}{1 - \beta \cos(\theta) \cos(\alpha)} \right)^2 \left(\frac{nJ_n(x)}{x} \right)^2 + J_n'(x)^2 \right] \quad (10)$$

With n_1 and n_2 the sum limits fixed by the resonant condition as $n_1 \sim \left(\frac{f_{obs}}{f_L} - \Delta f\right)(1 - \cos \theta \cos \alpha)\gamma$ rounded up to the nearest whole number and $n_2 \sim \left(\frac{f_{obs}}{f_L} + \Delta f\right)(1 - \cos \theta \cos \alpha)\gamma$ rounded down to the nearest whole number.

2.4. Integration of the Cyclo-Synchrotron Radiation Over an Isotropic Electron Distribution

As previously highlighted, the emission angular distribution exhibits significant variation with the particle's velocity. The synchrotron approximation which says that only electrons with a pitch angle $\alpha = \pm\gamma/2$ emit in the observer direction is not applicable to low energy electrons. Consequently, unlike the ultra-relativistic case, the power emitted by electrons in the cyclo-synchrotron regime must be integrated over all electron pitch angles $\alpha \in [0, \pi]$, as they all can emit in the observer direction. The normalized spectral power emitted by an isotropic electron distribution and received by an observer is shown in blue on Figure 2 and is given by:

$$P_f = \int_{\alpha} \frac{\partial^2(P/P_0)}{\partial\Omega\partial(f/f_L)} \sin(\alpha) d\alpha \quad (11)$$

At lower energy levels, Figures 2a and 2c show that the numerical results derived from Equation 11 significantly diverge from the results of the synchrotron formula given by Equation 3, by several decades at most frequencies for $\beta = 0.6$ (Figure 2a). Clearly, using the synchrotron approximation in this case could lead to overestimate the power emitted by trans-relativistic electrons.

For β greater than 0.9 (representing electrons with energies around 700 keV, Figure 2d), the two models converge closely, permitting the utilization of the synchrotron approximation. We also retrieve that the synchrotron approximation cannot be used at low frequency, typically $ff/L < 0.5$, even at high energy.

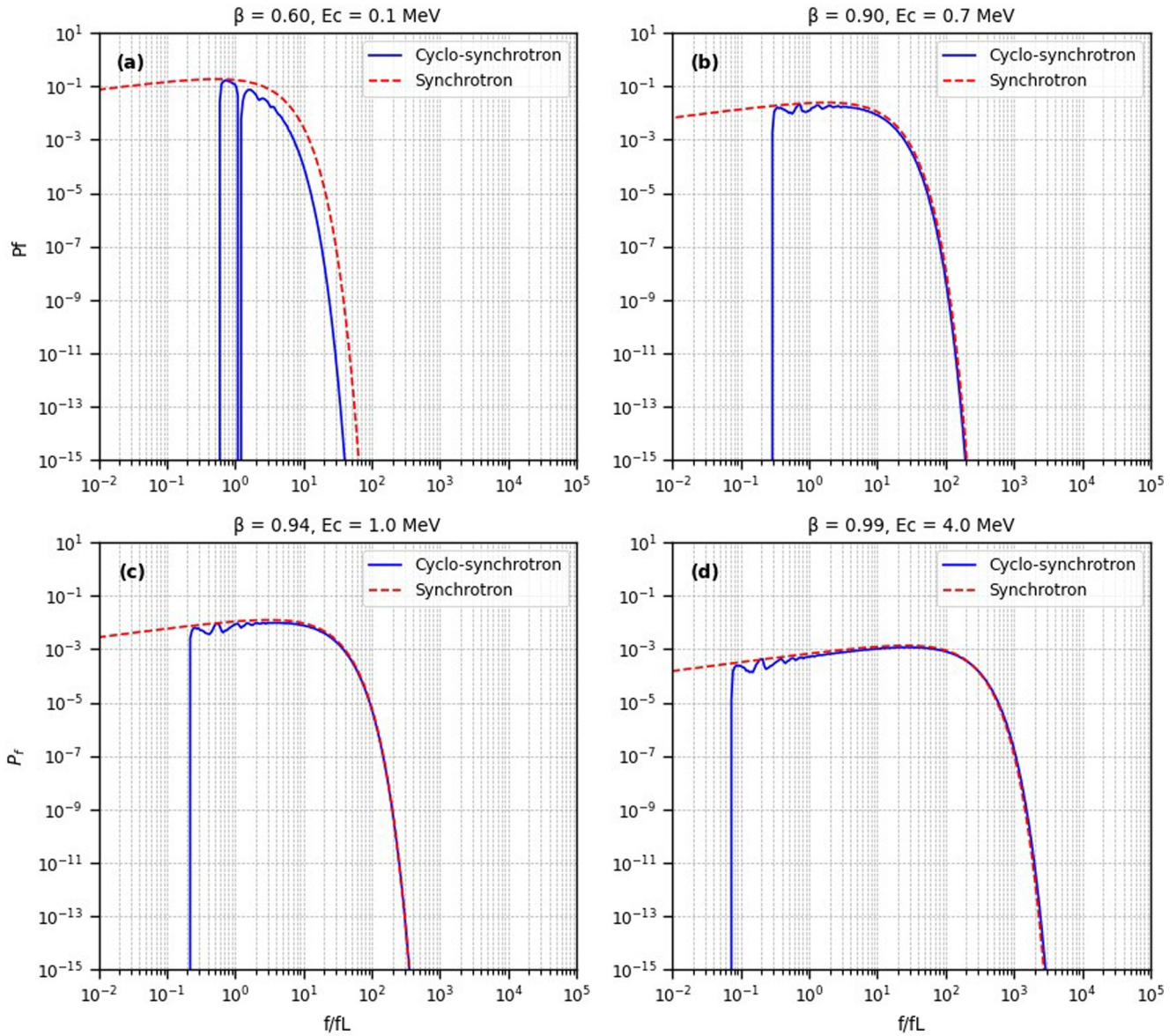


Figure 2. Plots of normalized emission as a function of f/fL for (a) $\beta = 0.6$, (b) $\beta = 0.9$, (c) $\beta = 0.94$, (d) $\beta = 0.99$ and an observation angle of $\theta = \pi/3$. The plain line corresponds to the cyclo-synchrotron emission of an isotropic distribution after integration over the pitch angle α given in Equation 11. The dashed line corresponds to the synchrotron emission given by Equation 3.

3. Methods: From the Radiation of an Electron to the Signal Received by a Lunar Observer

3.1. Emission From an Electron Population

Now that we know how to compute the power emitted by a single electron, we can determine the power emitted by a population of electrons with different energies and pitch angles as perceived by a distant observer.

We consider a population of electrons confined in an infinitesimal volume dV . The observer angle θ is defined as the angle between the magnetic field and the vector from dV to the observer. The spectral power emitted by the electron population and received by the observer is given by:

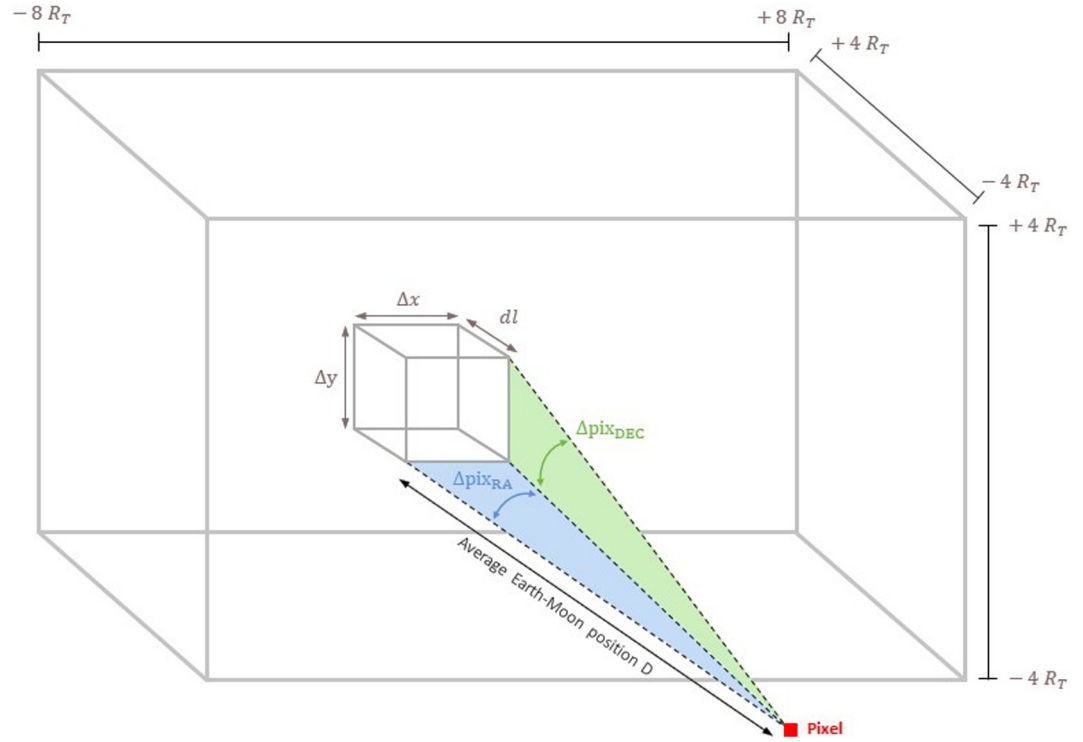


Figure 3. Definition of the computational volume and the angular size of pixels.

$$\frac{dP_f}{d\Omega dV} = \int_E \int_{\alpha} \frac{\partial^2 P}{\partial \Omega \partial f}(\alpha, \theta, E) N(\alpha, E) dE d\alpha \quad [W.Hz^{-1}.m^{-3}.str^{-1}] \quad (12)$$

$N(\alpha, E)$ corresponds to the number of electrons in volume dV in $MeV^{-1}.m^{-3}$ given by:

$$N(\alpha, E) = \frac{\sin(\alpha)}{c^3} 2\pi \sqrt{E_k(E_k + 2E_0)} (E_k + E_0) f \quad (13)$$

With f the electron distribution function in $MeV^{-3}.s^{-3}.sr^{-1}$, E_k the electron kinetic energy and E_0 the electron rest energy.

3.2. Cyclo-Synchrotron Radiation of the Terrestrial Radiation Belts Seen by a Distant Observer

Our objective is to simulate 2D images of the cyclo-synchrotron radiation emitted by electrons trapped in the radiation belts of Earth as detected by an instrument positioned on the lunar surface. Each pixel in the image represents the integral of radiation emitted by all the electrons along the observer line of sight (LOS). To calculate this value, we sum all contributions from elemental volumes distributed along the line of sight passing through the considered pixel.

It is important to note that the emission is assumed to be optically thin. However, radiative transfer effects could become significant, particularly at lower frequencies, and may require further investigation in future studies.

Our computations are conducted within a volume that encompasses the Earth and its radiation belts of ± 8 RE in the equatorial magnetic plane, and ± 4 RE along the magnetic axis as presented in Figure 3. We further subdivide this volume into smaller elemental units known as voxels. The size of these volumes is given by the integration step along the line of sight and the pixels size. The parameter Δpix_{RA} represents the angular size of a pixel in terms of right ascension, and Δpix_{DEC} represents the angular size of a pixel in terms of declination. A voxel is then defined by three dimensions $\Delta x = D.\Delta pix_{RA}$, $\Delta y = D.\Delta pix_{DEC}$ and dl , which represents the length dimension

along the line of sight. In this context, D corresponds to the distance between the considered volume and the observer, taken as the average Earth-Moon distance. With $dV = \Delta x * \Delta y * dl$, we get:

$$\frac{dP_f}{\partial\Omega} = \Delta x \Delta y \int_{LOS} \int_E \int_{\alpha} \frac{\partial^2 P}{\partial\Omega \partial f} N(\alpha, E) dE d\alpha dl \quad [W.Hz^{-1}.str^{-1}] \quad (14)$$

$$\frac{dP_f}{\partial\Omega} = D^2 \Delta pix_{RA} \Delta pix_{DEC} \int_{LOS} \int_E \int_{\alpha} \frac{\partial^2 P}{\partial\Omega \partial f} N(\alpha, E) dE d\alpha dl \quad (15)$$

The power received by a surface detector S at a distance D is defined as the power emitted by the electron population (Equation 15) multiplied by the solid angle S/D^2 . In our case, we want to obtain a power received by surface unit so the power received by a distant detector becomes:

$$\frac{dP_f}{dS} = \Delta pix_{RA} \Delta pix_{DEC} \int_{LOS} \int_E \int_{\alpha} \frac{\partial^2 P}{\partial\Omega \partial f} N(\alpha, E) dE d\alpha dl \quad [W.Hz^{-1}.m^{-2}] \quad (16)$$

We normalize dl by dividing by the Earth radius, resulting in $ds = dl/R_E$. Ultimately, the total spectral power per unit surface is expressed as:

$$\frac{dP_f}{dS}(1 \text{ pixel}) = R_E \Delta pix_{RA} \Delta pix_{DEC} \int_{LOS} \int_E \int_{\alpha} \frac{\partial^2 P}{\partial\Omega \partial f} N(\alpha, E) dE d\alpha ds \quad [W.Hz^{-1}.m^{-2}] \quad (17)$$

3.3. Input Data

In order to calculate the cyclo-synchrotron radiation emitted by electrons in the radiation belts, we need to know the distribution function of these electrons. We choose to use the electron fluxes simulated by the physical model Salammbô-3D developed at ONERA over several decades (Beutier & Boscher, 1995; Bourdarie & Maget, 2012). Salammbô-3D is a model designed for simulating electron and proton radiation belts. It operates by solving a time-dependent Fokker-Planck diffusion equation in the E , y , and L^* space, where E represents the particle's kinetic energy, y signifies the sine of the particle's equatorial pitch angle, and L^* is the particle's Roederer parameter. In the case of electrons, the model relies on various sub-models to evaluate different interactions occurring within the radiation belts, as detailed in (Brunet et al., 2023). The diffusion equation is solved using a finite volume Euler-implicit scheme (Brunet et al., 2023; Dahmen et al., 2020).

Every voxel within our computational volume corresponds to a position in the geocentric coordinate system and is associated with a L^* value calculated with IRBEM, along with a magnetic field value B calculated with the IGRF and Olson and Pfizer quiet models (Alken et al., 2021; Olson & Pfizer, 1974). The Salammbô-3D model provides unidirectional electron flux, considering the anisotropic distribution of electrons. Each individual voxel is associated with an electron flux value from which we can compute the density $N(\alpha, E)$ and simulate the cyclo-synchrotron radiation.

4. Results

In this section, we present the results of the new cyclo-synchrotron model applied for the first time to radiation belt emissions. In particular, we contrast the cyclo-synchrotron simulations with results obtained with the synchrotron approximation to highlight the importance of considering the cyclo-synchrotron formalism. Simulations are conducted at two representative dates and times: 16 March 2015 at 00:00 UTC and 26 March 2015 at 00:00 UTC, which are before and during a geomagnetic storm. Two kinds of results are presented: 2D images of the emitted power in Jansky/pixel and total emitted power in Jansky ($1 \text{ Jy} = 10^{-26} W.m^{-2}. Hz^{-1}$). The last one is the addition of the emitted power from each pixel of a 2D image.

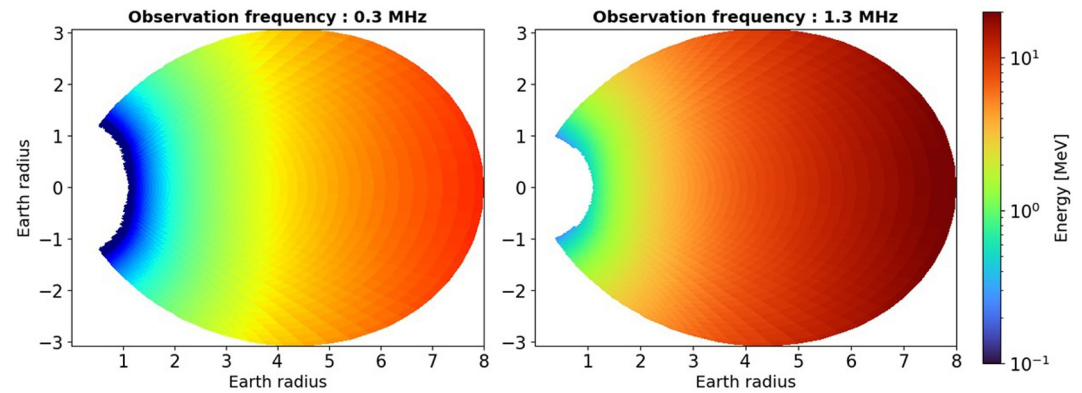


Figure 4. Maximum radiation energies for an observation frequency of 0.3 MHz (left) and 1.3 MHz (right).

4.1. Observation Frequencies

In this study, we focus on two specific observation frequencies, denoted as f_{obs} and equal to 0.3 and 1.3 MHz. These frequencies were selected to align with the energy levels of electrons within Earth's radiation belts. As illustrated in Figure 4, when $f_{obs} = 0.3$ MHz, the electron energies that emit the most intense radiation fall within the range of approximately 0.1–8 MeV. For $f_{obs} = 1.3$ MHz, our simulations target electrons at higher energy levels, with maximum radiation energies ranging from 1 to 20 MeV. The maps presented in Figure 4 were calculated considering that the energy of maximum emissivity is determined by $x = f_{obs}f_c = 0.29$ with f_c the critical frequency as defined in Equation 4 (Ginzburg & Syrovatsk, 1969).

4.2. Power Emitted by Different Ranges of Energy

When considering the development of a new model based on the cyclo-synchrotron equations, we wanted to quantify the emitted power across distinct electron energy ranges. The objective was to discern the relative importance of each energy range in contributing to the overall radiation output. Figure 5 represents the total power emitted for several energy ranges at an observation frequency of 1 MHz for two dates (26/03/2015 H00 (bottom) and 16/03/2015 H00 (top)). These plots show that most of the radiation is produced by the lower energy electrons, mostly because the flux of electrons quickly increases with decreasing energy. It is therefore critical to accurately compute the radiation of low-energy electrons.

Moreover, the simulations conducted on both date times reveal a significant distinction in intensity between the two models, cyclo-synchrotron and synchrotron, particularly within the 100 keV–1 MeV range. The most noticeable difference occurs in the lower energy range of 100–200 keV, where the total emitted power from the synchrotron model is more than three times higher than that from the cyclo-synchrotron model for the ‘quiet period’, and about four times higher during the ‘stormy period’.

The distribution of total emitted power across different energy ranges appears to exhibit considerable variability with the studied period and the chosen model. Table 1 illustrates that the new cyclo-synchrotron model appears to diminish the contribution of lower energies to the total power. Specifically, for electrons between 100 and 200 keV, the proportion decreases from 63% to 45% in the period following the peak of the magnetic storm and from 23% to 10% in the period preceding the storm. We can also observe that the contribution of electrons with energies between 100 keV and 1 MeV is significantly higher for March 26 during the geomagnetic storm.

Table 1 also highlights that emission from non-relativistic electrons represent around 90% of the total radiation during the “stormy period” of March 26, validating the importance of developing a new model to simulate the radiation more accurately at low energy during hazardous events.

4.3. 2D Brightness Images

For this study, we conducted simulations within a computational volume extending from $L^* = 1$ to $L^* = 8$ and our simulation grid was configured as $[N_r, N_\theta, N_\varphi] = [50, 100, 50]$. The results of our simulations are 2D brightness images of dimension 50×100 pixels of the total radiation intensity for a given observation frequency. The output

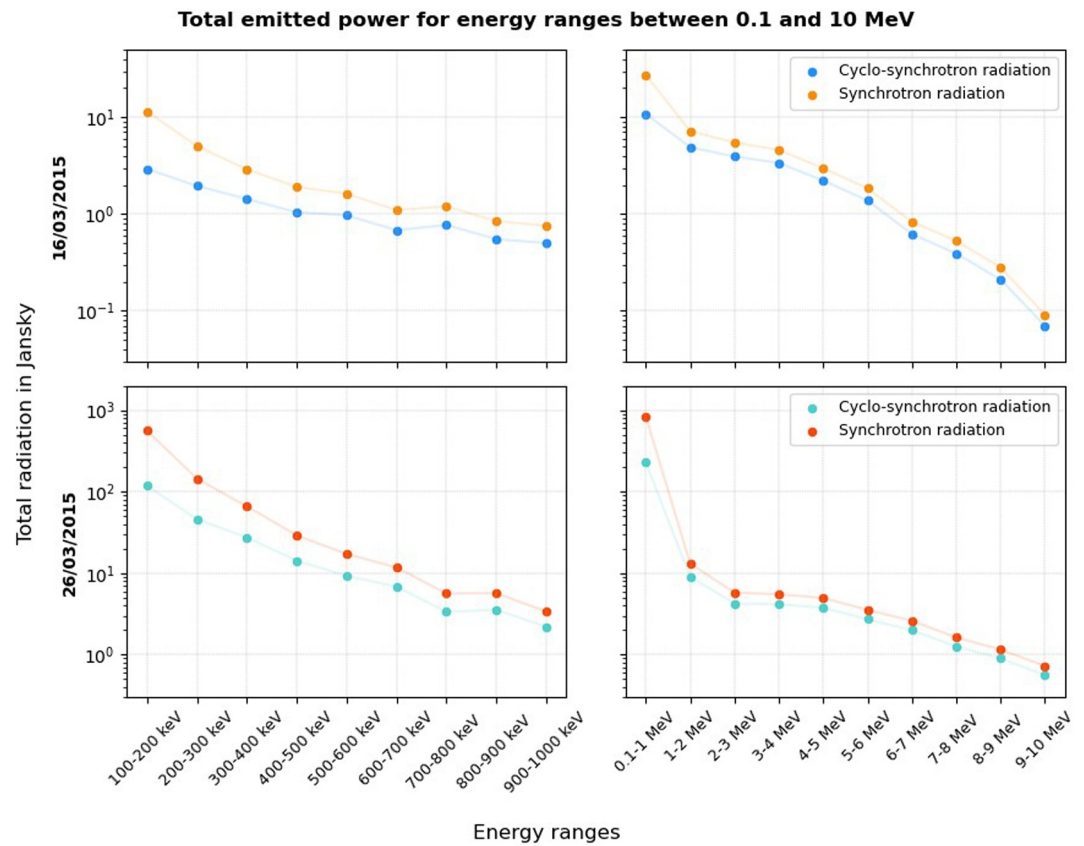


Figure 5. Total emitted power at 1 MHz for several energy ranges for the synchrotron model (in blue) and cyclo-synchrotron model (in orange) for the 26/03/2015 H00 (bottom) and 16/03/2015 H00 (top).

images provide visual representations of the spatial distribution and intensity of both cyclo-synchrotron and synchrotron radiation, measured in Jansky ($1 \text{ Jy} = 10^{-26} \text{ W} \cdot \text{m}^{-2} \cdot \text{Hz}^{-1}$).

Figures 6 and 7 show 2D brightness images generated by both the synchrotron and cyclo-synchrotron models, representing what would have been observable on 16/03/2015 and 2026/03/2015. Notably, these computations consider the Moon's declination and right ascension for the given dates. Their values have been provided by the *Institut de mécanique céleste et de calcul des éphémérides* (<https://ssp.imcce.fr/forms/ephemeris>). The images are presented in the Earth/Moon geographical plane, in which the dipole axis wobbles, and correspond to an observation frequency of 0.3 MHz (Figure 6) and 1.3 MHz (Figure 7).

The total radiation within an image is calculated as the sum of the intensity of all pixels of the image. As presented in Figures 6 and 7, the synchrotron model gives higher total radiation intensity. At $f_{obs} = 0.3 \text{ MHz}$, Figure 6 illustrates that the synchrotron model gives a total intensity 45% higher than the cyclo-synchrotron model for the “quiet time” and 75% higher during “storm time”. At $f_{obs} = 1.3 \text{ MHz}$, Figure 7 shows that the synchrotron model

Table 1
Contribution of Electron Energy Ranges to the Total Emitted Power Received by a Distant Observer

Energy ranges	Cyclo-synchrotron		Synchrotron	
	16 mars	26 mars	16 mars	26 mars
100–200 keV	10%	45%	23%	63%
100 keV to 1 MeV	39%	89%	52%	95%
1–10 MeV	61%	11%	47%	4%

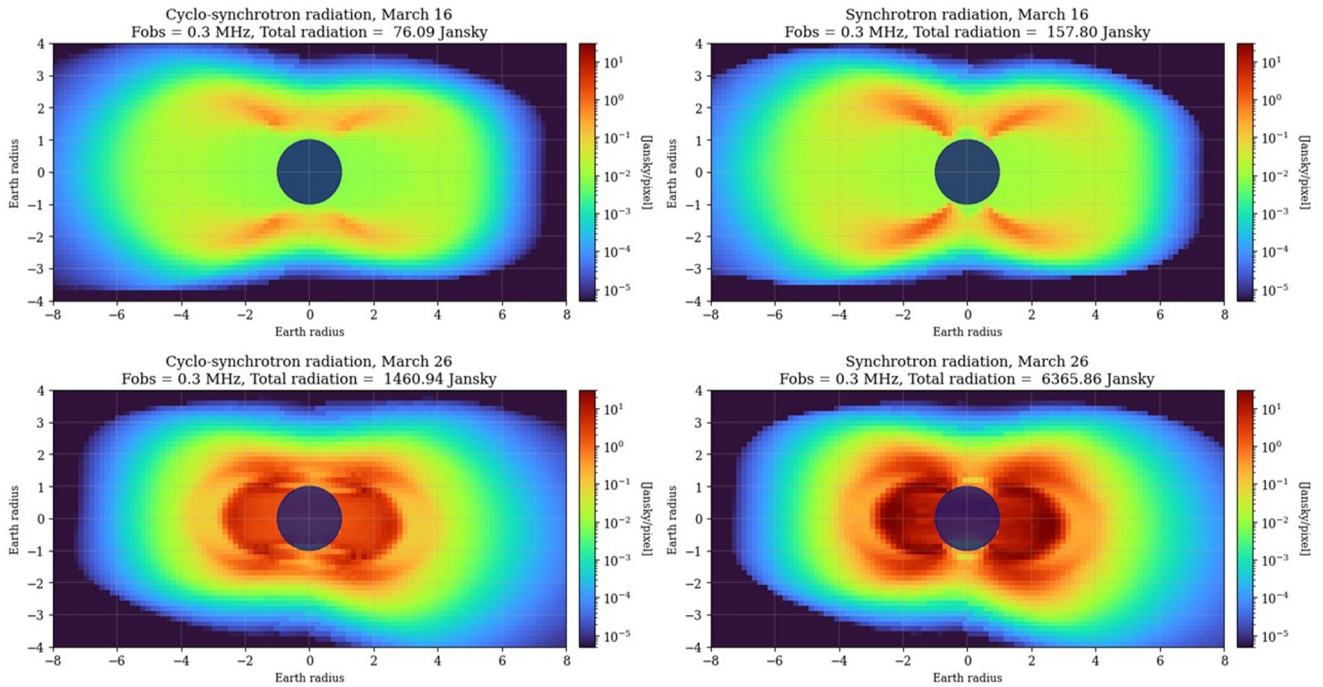


Figure 6. Brightness maps computed from Salammbô electron simulation with cyclo-synchrotron (left) and synchrotron (right) models for an observation frequency of 0.3 MHz for two dates: 16/03/2015 H00 (top) and 26/03/2015 H00 (bottom).

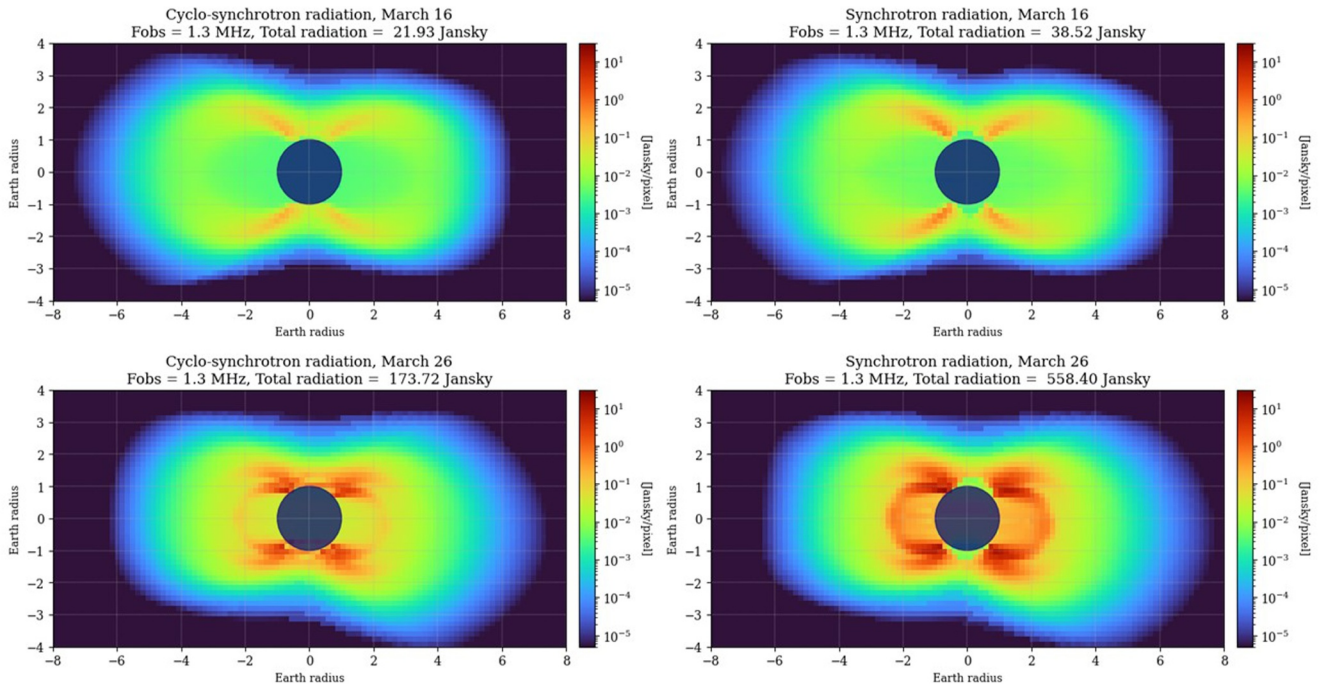


Figure 7. Brightness maps computed from Salammbô electron simulation with synchrotron (on the right) and cyclo-synchrotron (on the left) models for an observation frequency of 1.3 MHz for two dates: 26/03/2015 H00 (bottom) and 16/03/2015 H00 (top).

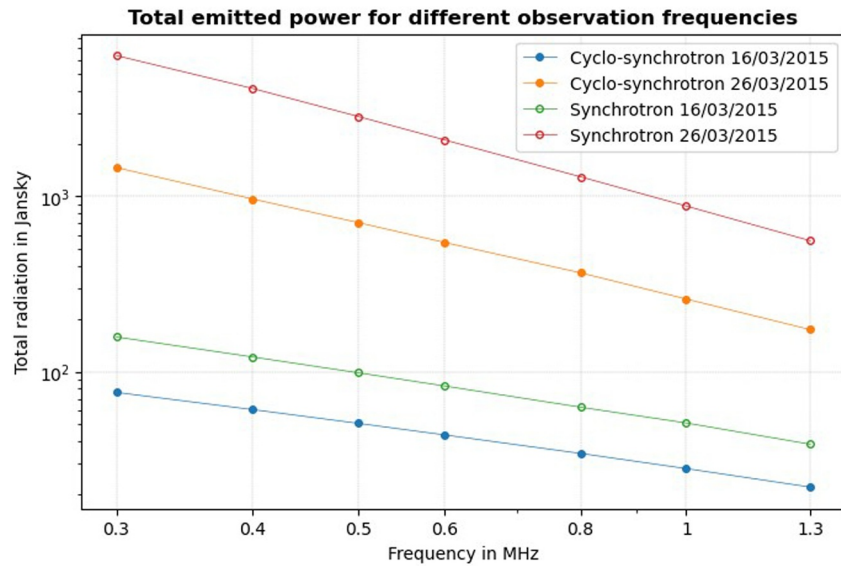


Figure 8. Total emitted power of 16/03/2015 and 26/03/2015 simulations for frequencies between 0.3 and 1.3 MHz.

gives a total intensity 35% higher than the cyclo-synchrotron model for the “quiet time” and 66% higher during “storm time”. While there are differences in intensity between the two models, the spatial distribution of radiation they produce shows similarities. Specifically, both models display peak intensities in Earth’s polar regions, specifically at the base of the magnetic L shells where the magnetic field is strongest. It is worth noting that cyclo-synchrotron intensities are directly proportional to the electron flux at a given energy level.

These figures also reveal a significant variation in the total intensity of radiation depending on the observation frequency. Simulations conducted at the 0.3 MHz observation frequency show higher global intensity. This may be attributed to the fact that, at this frequency, we are observing lower-energy electrons (Figure 5), which are more abundant in the Earth’s radiation belts.

4.4. Frequency Spectra

Figure 8 gives a summary of the simulation results for frequencies between 0.3 and 1.3 MHz. As a reminder, this frequency range was chosen to correspond to the energies of the electrons in the Earth’s magnetosphere.

As Figures 6 and 7, Figure 8 highlights the impact of the observation frequency on the radiation intensity. Cyclo-synchrotron and synchrotron results overall follow the same trend for both periods of time. In detail, on March 16, the total emitted power simulated by the cyclo-synchrotron model is 3.5 times higher at 0.3 MHz compared to 1.3 MHz, whereas this ratio is of 8.4 on March 26 due to the electron energy spectrum likely to be steeper during storm time.

5. Discussion

In 2020, Hegedus et al. introduced a preliminary model simulating the synchrotron radiation emitted by Earth’s radiation belts when observed from the lunar near side. This model was adapted from a previous synchrotron model created for the analysis of Jupiter’s radio emissions (Nénon, 2018; Santos Costa, 2001; Sicard, 2004). For these models, simulations were restricted to electrons with energies greater than 1 MeV ($\beta \sim 0.94$), limiting the scope to relativistic or quasi-relativistic electrons, thereby enabling the application of the synchrotron approximation.

Our new cyclo-synchrotron model builds upon the synchrotron model presented by Hegedus et al. (2020). Beyond the cyclo-synchrotron extension, several modifications have been integrated into our model. Our simulations are carried out in a brand-new energy range as we replaced the previous 1 MeV threshold with a lower limit of 100 keV, corresponding to the energy limit of validity of the Salammbô model. While Hegedus et al.’s simulations

approximated Earth's magnetic field using a simple dipole and described magnetic field lines using the McIlwain parameter L (McIlwain, 1961), in the new cyclo-synchrotron model presented here, the internal Earth magnetic field is simulated with the IGRF model, and the external magnetic field is obtained with the OPQUIET model (Alken et al., 2021; Olson & Pfitzer, 1974). Our model also uses the more precise Roederer parameter L^* (Roederer, 1967) and considers the exact position of the Moon in the calculations, including declination and right ascension.

Lowering the energy criterion in the synchrotron simulation tool had the consequence of generating brightness maps with very high intensities, with a considerable overestimation of the simulated signal. The transformation to cyclo-synchrotron radiation equations balanced this intensity increase. The cyclo-synchrotron model gives lower emitted power for the same energy range than synchrotron approximation. However, in our cyclo-synchrotron model energies between 100 keV and 1 MeV are taken into account and gives higher emitted power than in Hegedus et al., where only >1 MeV electrons are considered.

Figure 1 in Hegedus et al. shows a total emitted power of approximately 2 Jy for 1 November 2016 at an observation frequency of 0.736 MHz. Simulations using the new cyclo-synchrotron model under the same observational conditions give a total intensity of approximately 20 Jy. Extending the energy range to electrons over 100 keV reveals a tenfold increase compared to the preliminary model by Hegedus et al. Table 1 of Hegedus et al. presents the intensity of constant radio sources as seen from a lunar near-side observer. At 1 MHz, the lunar flux of the Sun's blackbody radiation is estimated at 4.84×10^{-2} Jy, and for the Earth's blackbody radiation, the flux is estimated to be 3×10^{-2} Jy. The new results presented in this paper indicate radiation intensities orders of magnitude higher than these sources. In 2020, Hegedus et al. concluded that the synchrotron radiation emitted by electrons over 1 MeV was observable with a lunar near-side instrument. The intensities presented in this paper suggest that cyclo-synchrotron radiation emitted by electrons over 100 keV is even more likely to be detectable. For comparison, at 1 MHz the intensity of Jupiter's radio emission is around 10^4 Jy as observed from near-Earth space. Despite its brightness compared to Earth's, the distance to Jupiter limits the spatial resolution of these observations.

6. Conclusions

This paper presents a significant advancement in the study of Earth's radiation belts through the development of a new cyclo-synchrotron model for simulating the emitted radiation as observed from the lunar near side. The limitations of the previous synchrotron model by Hegedus et al., 2020 have been addressed by extending the energy range to include electrons with energies between 100 keV and 1 MeV. This expansion allows for a more thorough understanding of the spatial and energy distribution of radiation belt electrons, providing a valuable tool for global coverage.

The cyclo-synchrotron model introduced in this paper incorporates improvements in the simulation process, such as the use of the IGRF model for the internal Earth magnetic field and the OPQUIET model for the external magnetic field. Additionally, the consideration of the precise position of the Moon, including declination and right ascension, enhances the accuracy of the calculations. These modifications result in a more realistic representation of the radiation emitted by electrons within Earth's radiation belts.

Comparative analysis between the synchrotron and cyclo-synchrotron models reveals the importance of lowering the energy criterion for a more accurate representation of the observed radiation. The cyclo-synchrotron model alleviates the overestimation observed in brightness maps generated by the synchrotron model, providing a more reliable estimation of the emitted power. Hegedus et al. (2020) have shown that a 1024-element 20-km radio array could resolve the terrestrial synchrotron radiation with an integration time of a few hours. As the radiation intensities of this previous work were underestimated, smaller radio arrays and faster integration times can be considered.

To conclude, monitoring the radiation belts with a lunar near side array would extend our space weather capabilities and improve our understanding of the radiation belt physics and dynamics.

Data Availability Statement

The right ascension and declination data for the Moon's position at specific times are calculated by the Institute for Celestial Mechanics and Ephemeris Calculation (IMCCE) and are accessible on their website at <https://ssp.imcce>.

[fr/forms/ephemeris](#) (Ephemeris - IMCCE, n.d.). The output images from both the Synchrotron and Cyclo-synchrotron models are available at <https://doi.org/10.57745/WEAFZK>. A Python script has been provided to facilitate the display of these images (Marc et al., 2024). The Salammbô, Synchrotron, and Cyclo-synchrotron models are proprietary models owned by ONERA, identified under the IDDN number IDDN.FR.001.470,003.000.S.X.2021.000.31235 (Dahmen, 2021).

Acknowledgments

We thank ESA for co-funding this study through Gwendoline Marc's PhD thesis (contract n°400013834522-NL-GLC).

References

- Alken, P., Thébault, E., Beggan, C. D., Amit, H., Aubert, J., Baerenzung, J., et al. (2021). International geomagnetic reference field: The thirteenth generation. *Earth Planets and Space*, 73(1), 49. <https://doi.org/10.1186/s40623-020-01288-x>
- Beutier, T., & Boscher, D. (1995). A three-dimensional analysis of the electron radiation belt by the Salammbô code. *Journal of Geophysical Research*, 100(A8), 14853–14861. <https://doi.org/10.1029/94JA03066>
- Bourdarie, S. A., & Maget, V. F. (2012). Electron radiation belt data assimilation with an ensemble Kalman filter relying on the Salammbô code. *Annales Geophysicae*, 30(6), 929–943. <https://doi.org/10.5194/angeo-30-929-2012>
- Brunet, A., Dahmen, N., Katsavrias, C., Santolík, O., Bernoux, G., Pierrard, V., et al. (2023). Improving the electron radiation belt nowcast and forecast using the SafeSpace data assimilation modeling pipeline. *Space Weather*, 21(8). <https://doi.org/10.1029/2022SW003377>
- Carr, T. D., Desch, M. D., & Alexander, J. K. (1983). Physics of the Jovian magnetosphere. 7. Phenomenology of magnetospheric radio emissions. In *Physics of the Jovian magnetosphere* (pp. 226–284). <https://doi.org/10.1017/CBO9780511564574.009>
- Dahmen, N. (2021). Salammbô model.
- Dahmen, N., Rogier, F., & Maget, V. (2020). On the modelling of highly anisotropic diffusion for electron radiation belt dynamic codes. *Computer Physics Communications*, 254, 107342. <https://doi.org/10.1016/j.cpc.2020.107342>
- de Pater, I. (1981). A comparison of the radio data and model calculations of Jupiter's synchrotron radiation. 1. The high energy electron distribution in Jupiter's inner magnetosphere. *Journal of Geophysical Research*, 86(A5), 3397–3422. <https://doi.org/10.1029/JA086iA05p03397>
- de Pater, I., & Kurth, W. S. (2007). Chapter 38—The solar system at radio wavelengths. In L.-A. McFadden, P. R. Weissman, & T. V. Johnson (Eds.), *Encyclopedia of the solar system* (2nd ed., pp. 695–718). Academic Press. <https://doi.org/10.1016/B978-012088589-3/50042-6>
- Ephemeris-IMCCE. (n.d.). [Dataset]. Retrieved from July 10, 2024, <https://ssp.imcce.fr/forms/ephemeris>
- Ginzburg, V. L., & Syrovatsk, S. I. (1969). Developments in the theory of synchrotron radiation and its reabsorption. *Annual Review of Astronomy and Astrophysics*, 7(1), 375–420. <https://doi.org/10.1146/annurev.aa.07.090169.002111>
- Girard, J. N., Zarka, P., Tasse, C., Hess, S., Pater, I., Santos-Costa, D., et al. (2016). Imaging Jupiter's radiation belts down to 127 MHz with LOFAR. *Astronomy and Astrophysics*, 587, A3. <https://doi.org/10.1051/0004-6361/201527518>
- Grießmeier, J.-M., Zarka, P., & Girard, J. N. (2011). Observation of planetary radio emissions using large arrays. *Radio Science*, 46(05), 1–9. <https://doi.org/10.1029/2011RS004752>
- Hegedus, A., Nénon, Q., Brunet, A., Kasper, J., Sicard, A., Cecconi, B., et al. (2020). Measuring the earth's synchrotron emission from radiation belts with a lunar near side radio array. *Radio Science*, 55(2), 1–20. <https://doi.org/10.1029/2019RS006891>
- Horne, R. B., Glauert, S. A., Meredith, N. P., Boscher, D., Maget, V., Heynderickx, D., & Pitchford, D. (2013). Space weather impacts on satellites and forecasting the Earth's electron radiation belts with SPACECAST. *Space Weather*, 11(4), 169–186. <https://doi.org/10.1002/swe.20023>
- Kuznetsov, A. A., & Fleishman, G. D. (2021). Ultimate fast gyrosynchrotron codes. *The Astrophysical Journal*, 922(2), 103. <https://doi.org/10.3847/1538-4357/ac29c0>
- Marc, G., Sicard, A., & Nénon, Q. (2024). Results of cyclo-synchrotron and synchrotron models with Python visualization program. [Dataset]. *Recherche Data Gow*. <https://doi.org/10.57745/WEAFZK>
- Marcowith, A., & Malzac, J. (2003). Cyclotron-synchrotron: Harmonic fitting functions in the non-relativistic and trans-relativistic regimes. *Astronomy and Astrophysics*, 409(1), 9–19. <https://doi.org/10.1051/0004-6361:20031060>
- McIlwain, C. E. (1961). Coordinates for mapping the distribution of magnetically trapped particles. *Journal of Geophysical Research* (1896-1977), 66(11), 3681–3691. <https://doi.org/10.1029/JZ066i011p03681>
- Nénon, Q. (2018). Etude et modélisation des ceintures de radiation de Jupiter. [Theses, Doctorat de l'Université de Toulouse délivré par l'Institut Supérieur de l'Aéronautique et de l'Espace (ISAE)] Retrieved from <https://hal.archives-ouvertes.fr/tel-01899128>
- Nénon, Q., Sicard, A., & Bourdarie, S. (2017). A new physical model of the electron radiation belts of Jupiter inside Europa's orbit. *Journal of Geophysical Research (Space Physics)*, 122(5), 5148–5167. <https://doi.org/10.1002/2017JA023893>
- Olson, W. P., & Pfizter, K. A. (1974). A quantitative model of the magnetospheric magnetic field. *Journal of Geophysical Research* (1896-1977), 79(25), 3739–3748. <https://doi.org/10.1029/JA079i025p03739>
- Roederer, J. G. (1967). On the adiabatic motion of energetic particles in a model magnetosphere. *Journal of Geophysical Research* (1896-1977), 72(3), 981–992. <https://doi.org/10.1029/JZ072i003p00981>
- Rybicki, G. B., & Lightman, A. P. (1979). In *Radiative processes in astrophysics* (pp. 167–186). A Wiley-Interscience Publication. Retrieved from <https://ui.adsabs.harvard.edu/abs/1979rpa..book>
- Santos Costa, D. (2001). Modélisation des ceintures de radiation d'électrons de Jupiter internes à Io. [These de doctorat, École nationale supérieure de l'aéronautique et de l'espace (Toulouse ; 1972-2007)] <https://www.theses.fr/2001ESAE0010>
- Santos-Costa, D., Bolton, S. J., Thorne, R. M., Miyoshi, Y., & Levin, S. M. (2008). Investigating the origins of the Jovian decimetric emission's variability. *Journal of Geophysical Research (Space Physics)*, 113(A1), A01204. <https://doi.org/10.1029/2007JA012396>
- Schott, G. A., & with Gerstein - University of Toronto. (1912). *Electromagnetic radiation and the mechanical reactions arising from it, being an adams prize essay in the university of cambridge*. Univ. Press. Retrieved from <http://archive.org/details/electromagneticr00schouft>
- Schwinger, J. (1949). On the classical radiation of accelerated electrons. *Physical Review*, 75(12), 1912–1925. <https://doi.org/10.1103/PhysRev.75.1912>
- Sicard, A. (2004). Modélisation des ceintures de radiation d'électrons et d'ions de Jupiter. [These de doctorat, École nationale supérieure de l'aéronautique et de l'espace (Toulouse ; 1972-2007)] Retrieved from <https://www.theses.fr/2004ESAE0007>
- Sicard, A., Bourdarie, S., Krupp, N., Lagg, A., Boscher, D., Santos-Costa, D., et al. (2004). Long-term dynamics of the inner Jovian electron radiation belts. *Advances in Space Research*, 33(11), 2039–2044. <https://doi.org/10.1016/j.asr.2003.04.053>
- Wolfe, B., & Melia, F. (2006). Transrelativistic synchrotron emissivity, cross section, and polarization. *The Astrophysical Journal*, 637(1), 313–321. <https://doi.org/10.1086/497890>